Lab on a Chip

PAPER

Check for updates

Cite this: *Lab Chip*, 2022, **22**, 2832

Kinetic analysis of the growth behavior of perovskite $CsPbBr_3$ nanocrystals in a microfluidic system†

Xiaobing Tang and Fuqian Yang *

Received 9th April 2022,
Accepted 2nd July 2022

DOI: 10.1039/d2lc00331g

rsc.li/loc

Understanding the growth behavior of nanoparticles and semiconductor nanocrystals under dynamic environments is of profound importance in controlling the sizes and uniformity of the prepared nanoparticles and semiconductor nanocrystals. In this work, we develop a relation between the bandgap (the photoluminescence peak wavelength) of semiconductor nanocrystals and the total flow rate for the synthesis of semiconductor nanocrystals in microfluidic systems under the framework of the quantum confinement effect without the contribution of Coulomb interaction. Using this relation, we analyze the growth behavior of $CsPbBr_3$ nanocrystals synthesized in a microfluidic system by an antisolvent method in the temperature range of 303 to 363 K. The results demonstrate that the square of the average size of the $CsPbBr_3$ nanocrystals is inversely proportional to the total flow rate and support the developed relation. The activation energy for the rate process controlling the growth of the $CsPbBr_3$ nanocrystals in the microfluidic system is 2.05 kJ mol^{-1}. Increasing the synthesis temperature widens the size distribution of the $CsPbBr_3$ NCs prepared in the microfluidic system. The method developed in this work provides a simple approach to use photoluminescent characteristics to *in situ* monitor and analyze the growth of semiconductor nanocrystals under dynamic environments.

Introduction

Microfluidics, derived originally from microelectronic fabrication processes and microelectromechanical devices and systems, is an active research field for lab-on-a-chip technology and has become an important technique in bioengineering, chemical analysis, optoelectronics and other fields. Microfluidic-based chips have been used in applications of medical diagnostics,[1–3] biological detection,[4] optoelectronic monitoring,[5,6] three-dimensional printing,[7–9] synthesis of nanoparticles[10,11] and so forth, attributed to a wide range of merits including low cost, high sensitivity, less reagent consumption, *etc.*

Semiconductor nanocrystals (NCs), also referred to as quantum dots (QDs), which exhibit the quantum confinement effect due to their characteristic dimensions being comparable to (or smaller than) the exciton Bohr radius[12] or electrons being constrained to a domain comparable to their de Broglie wavelength,[13] have a variety of applications in optoelectronics, including light-emitting diodes (LEDs), solar cells, liquid crystals display (LCD), *etc.*[13,14] Over the past few decades, there have been extensive studies on the synthesis and application of cadmium (Cd)-based chalcogenides NCs. However, the costly and complex synthesis processes for core–shell NCs of high stability have hindered their industrialization and commercialization. On the other hand, lead halide perovskite nanocrystals (PeNCs) with lower cost and more facile synthesis processes than conventional Cd-based chalcogenide NCs have attracted wide interest for applications in solar cells[15,16] and have been considered as potential materials for next-generation high-performance lighting and displays due to their huge merits of high color purity, high brightness, high defect tolerance and so forth.[14,17,18] Additionally, all-inorganic (commonly Cs-based) PeNCs are more promising than organic–inorganic hybrid (commonly CH_3NH_3 (MA) or $CH(NH_2)_2$ (FA)-based) PeNCs in optoelectronic applications due to their higher chemical stability.[19,20]

There are reports on the use of microfluidic systems to synthesize all-inorganic PeNCs.[21–23] Microfluidics provides a highly efficient, reproducible and continuous route for the synthesis of PeNCs and outperforms conventional batch-mode methods of small amounts, which suffer from issues associated with size control and distribution from batch to batch.[24] Compared with the conventional small batch-mode methods for fundamental research, microfluidics is an efficient method for large-scale preparation of PeNCs.[24]

Materials Program, Department of Chemical and Materials Engineering, University of Kentucky, Lexington, KY 40506, USA. E-mail: fuqian.yang@uky.edu

† Electronic supplementary information (ESI) available. See DOI: https://doi.org/10.1039/d2lc00331g

This journal is © The Royal Society of Chemistry 2022

Microfluidic synthesis also possesses the merits of easy temperature control, large heat and mass transfer, efficient mixing, *etc.*[25] Using an automated microfluidic platform, Epps *et al.*[26] were able to synthesize $CsPbBr_3$ QDs. Lignos *et al.*[27] synthesized $CsPbX_3$ (X = Br, I, Cl, Cl/Br and Br/I) NCs *via* a droplet-based microfluidic platform and studied the effects of the molar ratios of Pb to Cs and I to Br, temperature and reaction time on the photoluminescence (PL) emission of the as-obtained perovskite NCs. Incorporating NCs into polymers with a microfluidic-spinning microreactor, Ma *et al.*[28] produced poly(methyl) methacrylate (PMMA)–$CsPbBr_3$ nanocomposites and studied the fluorescence of the nanocomposites with a focus on optoelectronic applications, including LEDs, microfibers and LCDs. Zhang *et al.*[23] observed five different cross-sections of all-inorganic PeNCs prepared in a PTFE-based microfluidic system. Applying artificial intelligence in the analysis of the synthesis of $CsPbBr_3$ QDs in a three-phase microfluidic platform, Abolhasani *et al.*[29] performed closed-loop formulation optimization and were able to improve the continuous manufacturing. Li *et al.*[30] investigated the dependence of the PL characteristics on the reaction temperature, ligand, and alkyl-chain structure of the ligand. Geng *et al.*[31] demonstrated the effects of residence time on the evolution of the morphology and crystal size of the $CsPbBr_3$ NCs synthesized in a microfluidic system. Guo *et al.*[32] prepared $CsPbI_3$–mesoporous SiO_2 nanocomposites *via* a microfluidic system made from a polytetrafluoroethylene (PTFE) capillary. They did not provide any information about the synthesis temperatures. Bao *et al.*[33] prepared Cs_4PbBr_6 perovskite microcrystals in a microfluidic system at 150 °C. Note that all of the above studies required a high temperature of around 400 K in the synthesis of the PeNCs for a variety of applications, including microfibers,[34,35] lasers,[21] and barcodes.[36]

Recently, Abdel-Latif *et al.*[37] proposed a halide exchange apparatus for the room-temperature synthesis of Cs-based inorganic perovskite QDs of various emission wavelengths, which involves anion exchange, in a microfluidic system. However, the preparation of the materials was complicated and involved an oil-bath process at 433 K and evaporation at 393 K. Kang *et al.*[38] used halide exchange to synthesize $CsPb(X/Y)_3$ (X = Br, Y = Cl, I) NCs, which exhibited light emission of 410–630 nm as the emission wavelength. Maceiczyk *et al.*[39] evaluated the effect of growth time on the size distribution of CdSe NCs synthesized in a microfluidic platform. Epps *et al.*[26] and Tang *et al.*[40] reported the effect of growth time on the wavelength of $CsPbBr_3$ NCs. Zhang *et al.*[41] demonstrated the morphological evolution of $CsPbBr_3$ NCs at a temperature of 50–120 °C.

In addition to all-inorganic $CsPbX_3$ NCs, organic–inorganic hybrid perovskite NCs have also been synthesized by microfluidics. Maceiczyk *et al.*[42] prepared $FAPbX_3$ (X = Br, I) NCs and tuned the emission wavelength by controlling the ratio of Br to I and temperature. Lignos *et al.* fabricated $FAPbX_3$ (X = Cl, Br) NCs[43] with the emission wavelength in the range of 440–515 nm by changing the percentage of halide (Cl) element and $Cs_xFA_{1-x}Pb(Br_{1-y}I_y)_3$ NCs[44] with the emission wavelength in the range of 700–800 nm by adding Br ions and the emission wavelength in the range of 690–780 nm by controlling the ratios of FA to Pb and Cs to Pb. Bezinge *et al.*[45] prepared $(Cs/FA)Pb(I/Br)_3$ and $(Rb/Cs/FA)Pb(I/Br)_3$ NCs with a self-optimizing algorithm in controlling the synthesis of NCs with defined characteristics in the light emission.

Understanding the growth kinetics/behavior of semiconductor NCs is critically important in controllable synthesis of semiconductor NCs. Yang[46] proposed a simple relation correlating the PL (photoluminescence) peak wavelength to the growth time without electrostatic interaction, which is supported by the experimental data for the growth of CdSe and CdSe/ZnS NCs given by Karim *et al.*[47] However, few studies have been focused on the growth behavior of PeNCs in microfluidic systems/microreactors. The understanding of the growth of PeNCs in microfluidic systems/microreactors remains elusive. There is a great need to develop a feasible method to study the growth behavior of PeNCs in microfluidic systems in order to control and optimize the synthesis of PeNCs.

Li *et al.*[48] reported an antisolvent method for the synthesis of PeNCs at room temperature. The formation of PeNCs in the antisolvent method is based on a reprecipitation process when an antisolvent (nonpolar or poor solvent) is added into the precursor solution prepared with a polar (good) solvent, due to much smaller solubility of ions in the antisolvent than in the precursor solution.[18,48] Such an approach is energy-saving and has the potential of being integrated in microfluidic systems. Using an antisolvent approach in a three-phase microfluidic system, Wei *et al.*[49] synthesized $CsPbBr_3$ NCs and studied the effect of the velocity ratios of different phases on the crystallinity and size of the NCs. Lin *et al.*[50] fabricated Ce^{3+}-doped $CsPbBr_3$ NCs and tuned the doping concentration by altering the flow rate. Ng *et al.*[51] investigated the effect of the precursor mixing rate on the synthesis of $CsPbBr_3$ NCs by an antisolvent approach in a microfluidic platform. Few works have assessed the growth behavior of PeNCs synthesized in microfluidic systems. The purpose of this work is to analyze the growth behavior of $CsPbBr_3$ NCs prepared by an antisolvent method in a microfluidic system by evaluating the dependences of the PL characteristics/bandgaps of the prepared $CsPbBr_3$ NCs on the synthesis temperature and the total flow rate through the microfluidic system. Using the PL characteristics of the prepared $CsPbBr_3$ NCs, we determine the activation energy for the rate process controlling the growth of the prepared $CsPbBr_3$ NCs and observe that a higher total flow rate can reduce the dispersity of the $CsPbBr_3$ NCs.

Experimental details

Chemicals

The materials used were CsBr (99.9%, Beantown Chemical), $PbBr_2$ (>98%, Strem Chemicals Inc.), *N*,*N*-dimethylformamide

(DMF) (VWR), oleylamine (OAm) (>50%, TCI America), oleic acid (OA) (Ward's Science), and toluene (VWR). The as-received materials were used without any purification.

Preparation of the precursor solution for $CsPbBr_3$ NCs

A solution of 10 mL DMF, 1 mL OA and 0.5 mL OAm was placed in a glass vial with equimolar (0.4 mol) CsBr and $PbBr_2$ powders to form a mixture. The precursor solution was prepared after heating the mixture at 303 K overnight under vigorous stirring.

Microfluidic platform

Fig. 1 shows schematically the set-up of the microfluidics platform used in this work. Two syringe pumps (Harvard Apparatus) were used to support two syringes. The two syringes were filled with the precursor solution and antisolvent (toluene), respectively. A mini-vial (1 cm^3 in volume), which was connected to the two syringes through two PTFE capillaries (0.8 mm in inner diameter and 80 cm in length) and fixed to a temperature-controllable hot plate, was used as the miniaturized reactor for the formation and growth of $CsPbBr_3$ NCs. A third capillary of 0.8 mm inner diameter and 60 cm length was used to transport the liquid (the precursor solution and antisolvent) from the miniaturized reactor to a large glass vial. Continuous growth of $CsPbBr_3$ NCs occurred also in the third capillary tube; a large glass vial placed in a cooling system (ice-water bath) was used to collect the suspension consisting of $CsPbBr_3$ NCs. The flow rates of the precursor solution and antisolvent in the capillary tubes were controlled by the syringe pumps.

Synthesis of $CsPbBr_3$ NCs in the microfluidic platform

The synthesis of $CsPbBr_3$ NCs was based on an antisolvent method,[48] which is also referred to as a reprecipitation method.[52] Specifically, the perovskite precursor solution and toluene (antisolvent) were flowed into the miniaturized reactor with a flow rate ratio of 1 to 20 (perovskite precursor solution to toluene) to maintain the same volume ratio of 1 : 20 for different flow rates. The two solutions were mixed in the miniaturized reactor (the mini-vial), leading immediately to the formation of $CsPbBr_3$ NCs. It took less than three seconds to form $CsPbBr_3$ NCs.[48] The mixed solution with the formed $CsPbBr_3$ NCs was then flowed from the miniaturized reactor into the large glass vial, which was placed in an ice-water bath, for the collection of the formed $CsPbBr_3$ NCs. The ice-water bath was used to prevent the formed $CsPbBr_3$ NCs from undergoing further growth[12] and rapid fouling due to the increase in the NC sizes.[53] Note that the growth of NCs is related to the frequency of monomers attaching to the clusters/NCs, *i.e.*, the higher the frequency, the larger the NCs.[54] The attachment frequency increases with increasing temperature.[54] Lowering the temperature of a NC solution can retard the growth of NCs in the solution to some extent.

It should be noted that precipitation is a universal phenomenon during the preparation of nanocrystals, which is due to the increase in the sizes of the NCs through the coalescence (growth) of NCs. It generally uses a cooling system to lower the synthesis temperature and limit the growth (coalescence) of NCs. The rapid fouling and precipitation of NCs in a microfluidic system is dependent on the flow rate, growth temperature and relative size of the NCs to the diameter of the flow channels. Increasing the flow speed, reducing the concentration of NCs and lowering the growth temperature can hinder the rapid fouling and precipitation of NCs in a microfluidic system. Note that fouling and precipitation of NCs in two-phase or multi-phase flow systems can also occur, depending on the sizes of the NCs possibly grown in the system (droplets).

Four different flow rates of 0.05, 0.10, 0.20 and 0.30 mL min^{-1} were used for the precursor solution. The synthesis of the $CsPbBr_3$ NCs in the microfluidic platform was conducted

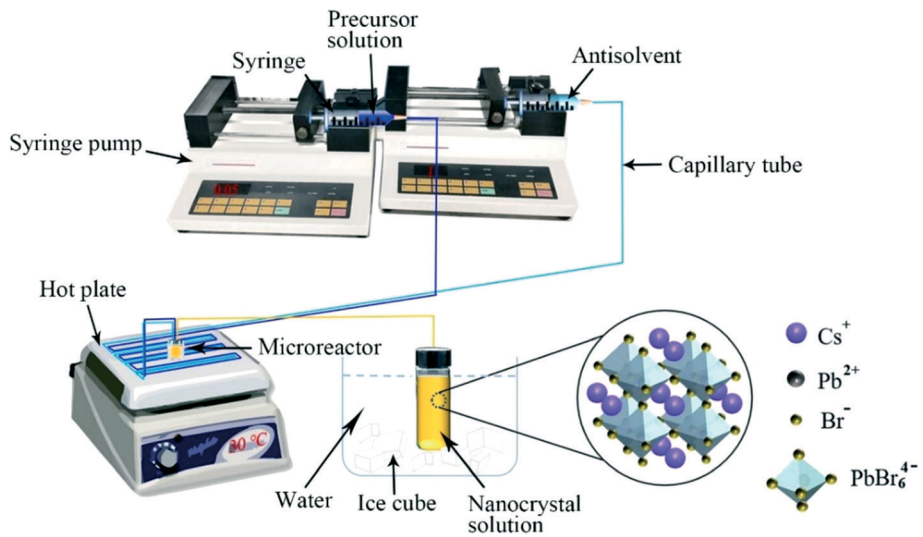

Fig. 1 Schematic of the microfluidic platform used for the preparation of $CsPbBr_3$ NCs of cubic structure as circled by the solid black line.

 This journal is © The Royal Society of Chemistry 2022

at four different temperatures of 303, 323, 343 and 363 K. Both the syringe pumps with the precursor solution and antisolvent were pre-heated to a pre-determined reaction temperature prior to the solutions being flowed into the miniaturized reactor, and the miniaturized reactor and the capillary connecting the miniaturized reactor to the NC-collection vial were placed on a hot plate and maintained at the pre-determined reaction temperature. Most of the capillaries connecting the pumps to the miniaturized reactor were placed on the hot plate and maintained at the pre-determined reaction temperature. This limited the heat loss and was able to maintain the reaction temperature to a reasonable degree. A piece of asbestos ($50 \times 50 \times 1.7$ cm^3) was used to cover the system (pump, capillaries and hot plate) to maintain a stable and uniform temperature. It should be noted that some NCs might not flow out of the miniaturized reactor immediately at a low flow rate. However, this did not likely play any important role in the growth of the NCs since the analysis was based on the average size of NCs. A batch-to-batch preparation of $CsPbBr_3$ NCs was carried out for 5 times, and the average results from the five tests were used in the kinetic analysis. To evaluate the feasibility of the proposed microfluidic platform for long-term continuous manufacturing of $CsPbBr_3$ NCs, the batch-to-batch preparation of $CsPbBr_3$ NCs on the same microfluidic system under the same growth conditions was performed continuously (for five times) without cleaning the system. No blockage of the microfluidic system occurred.

Characterization

PL characterization of the liquid solution with the formed $CsPbBr_3$ NCs in the large glass vial was conducted immediately on a miniature spectrometer (Ocean optics) after the completion of the flow. The XRD (X-ray diffraction) characterization of the crystal structure of the formed $CsPbBr_3$ NCs was performed on a diffractometer (Siemens D-500) with CuK_α radiation (λ = 1.54060 Å). The sample preparation for the XRD characterization of the formed $CsPbBr_3$ NCs involved the centrifugation of the liquid solution with the formed $CsPbBr_3$ NCs at 8000 rpm for 5 min and the evaporation of the solvent residuals in the collected sediments from the centrifugation in air. Note that the coalescence of the formed $CsPbBr_3$ NCs likely occurred during the sample preparation for the XRD characterization. The geometrical characteristics of the formed $CsPbBr_3$ NCs were examined on a transmission electron microscope (TEM) (Thermo-scientific Talos F200X) at an accelerating voltage of 200 kV. The sample for the TEM characterization was obtained directly from the liquid solution with the formed $CsPbBr_3$ NCs in the large glass vial immediately after the end of the synthesis, in contrast to the sample preparation for the XRD characterization, which likely limited the coalescence effect on the sizes of the formed $CsPbBr_3$ NCs.

Results

The formation of $CsPbBr_3$ NCs is dependent on the solubility of $CsPbBr_3$ in a solvent. CsBr, $PbBr_2$ and $CsPbBr_3$ crystals have large solubilities in the polar solvent DMF, resulting in the presence of Cs^+, Pb^{2+} and Br^- in the precursor solution. When the precursor solution is mixed with the nonpolar solvent toluene, the nucleation of the $CsPbBr_3$ clusters occurs, leading to the formation of $CsPbBr_3$ NCs. OA and OAm interact with the $CsPbBr_3$ NCs and form a protective layer (ligands) on the $CsPbBr_3$ NCs (NC–ligand structure) to hinder the growth of the $CsPbBr_3$ NCs and cause the dispersion of the NC–ligand structures in toluene.

The total flow rate is defined as the summation of the flow rate of the precursor solution and the flow rate of toluene. We have total flow rates of 1.05, 2.1, 4.2 and 6.3 mL min^{-1}, corresponding to the 0.05, 0.10, 0.20 and 0.30 mL min^{-1} flow rates of the precursor solution, respectively.

Fig. 2 presents TEM images of the $CsPbBr_3$ NCs formed at four different temperatures for the total flow rate of 1.05 mL min^{-1}. It is evident that the size of the NCs increases with increasing temperature. Using the TEM images, the size distribution of the formed $CsPbBr_3$ NCs is determined and presented in Fig. S1 in the ESI.† From the size distribution of the formed $CsPbBr_3$ NCs, we obtain average sizes of $\sim$13 ± 2, $\sim$20 ± 3, $\sim$27 ± 2 and $\sim$34 ± 4 nm for the $CsPbBr_3$ NCs formed at the four different temperatures of 303, 323, 343 and 363 K, respectively, for the total flow rate of 1.05 mL min^{-1}.

Fig. 3 depicts the XRD patterns of the formed $CsPbBr_3$ NCs at four different temperatures for different total flow rates. All of the XRD patterns are generally in good agreement with PDF card#54-0752, confirming the cubic structure of the formed $CsPbBr_3$ NCs. Such a result suggests that the crystal structure of the formed $CsPbBr_3$ NCs is independent of the temperature and flow rate used in this work. The two theta angles of $\sim$15°, $\sim$22°, $\sim$31°, $\sim$34°, $\sim$38°, $\sim$44° and $\sim$47° for the XRD peaks presented in Fig. 3 correspond to the (100), (110), (200), (210), (211), (220) and (300) planes, respectively. Note that the XRD-peak intensities increase with the increase of the temperature and the full width at half maximum (FWHM) of the peak is smaller at a higher temperature. The decrease of the FWHM with increasing temperature can be likely attributed to the increase of the NC size.[55] A large lattice strain due to the defects introduced at a high temperature can also lead to a large FWHM of the XRD peak.

Using the Scherrer equation, $D = K\lambda/\beta\cos\theta$ (D, K, λ, β and θ are average crystallite size, shape factor, wavelength of X-rays, half width of the XRD peak and diffraction angle, respectively), we calculate the average sizes of the $CsPbBr_3$ NCs formed at different temperatures for different flow rates. The average sizes of the $CsPbBr_3$ NCs are listed in Table S1 in the ESI.† It is evident that the average crystal size of the formed $CsPbBr_3$ NCs increases with the decrease of the flow rate at the same synthesis temperature and increases with

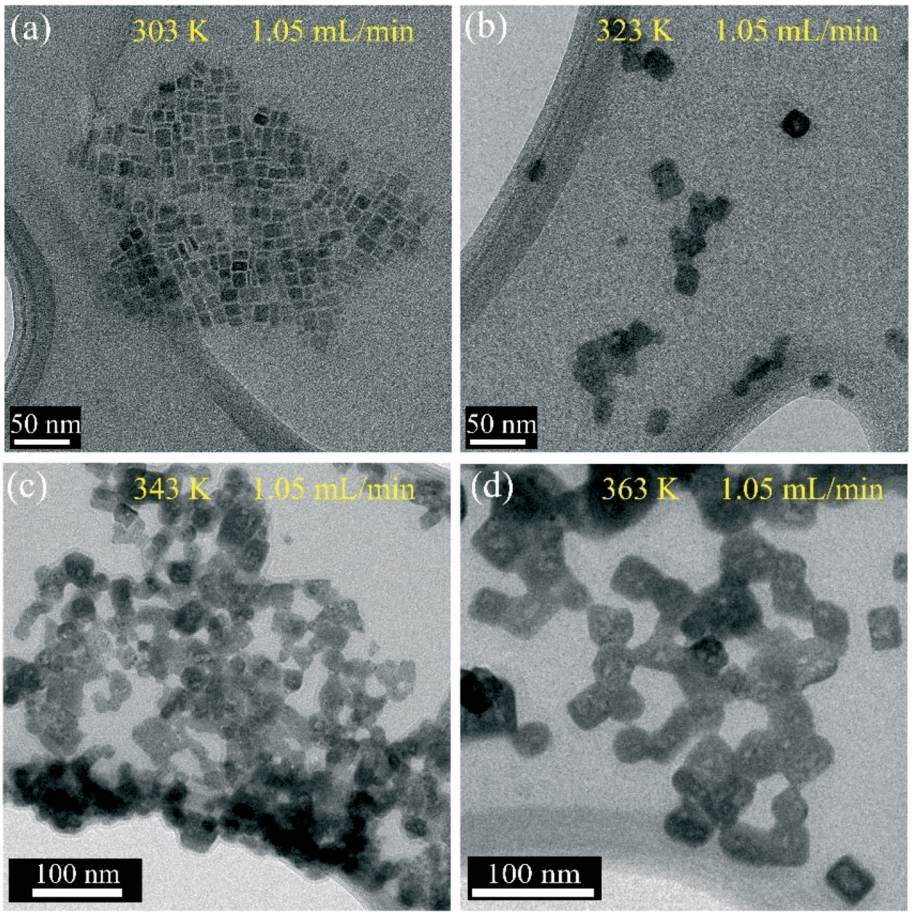

Fig. 2 TEM images of the $CsPbBr_3$ NCs formed at four different temperatures for the total flow rate of 1.05 mL min^{-1}: (a) 303 K, (b) 323 K, (c) 343 K, and (d) 363 K (total flow rate = flow rate of precursor solution + flow rate of toluene).

the increase of the synthesis temperature for the same flow rate, as expected. Note that there are some differences between the average crystal sizes of the formed $CsPbBr_3$ NCs determined from the TEM images and the corresponding ones determined from the XRD analysis for the total flow rate of 1.05 mL min^{-1}. Such differences can be likely attributed to the following reasons. TEM images are two-dimensional and the crystal size in the depth direction is unknown. The average crystal size is calculated from two-dimensional information. TEM images only provide the information of local area with small amounts of samples. XRD patterns contain three-dimensional information from large amounts of samples, and the average crystal size is calculated from much larger numbers of crystals.

Fig. 4 shows optical images of the suspensions of the $CsPbBr_3$ NCs under UV light of 365 nm wavelength, which were prepared with different total flow rates at different temperatures. The $CsPbBr_3$ NCs in the solution prepared at 303 K with the total flow rate of 6.3 mL min^{-1} emitted blue-green light (483 nm wavelength). Increasing the synthesis temperature and/or decreasing the flow rate causes an increase in the emission wavelength of the $CsPbBr_3$ NCs in the solution. For example, the $CsPbBr_3$ NCs in the solution prepared at 363 K with the total flow rate of 1.05 mL min^{-1} emitted yellow-green light (519 nm wavelength). Such a change in the color of the emission light can be attributed to the size dependence of the $CsPbBr_3$ NCs on the synthesis conditions, including temperature and flow rate.

The normalized PL spectra of the prepared $CsPbBr_3$ NCs are presented in Fig. 5 and S2 in the ESI.† According to Fig. 5a–d, increasing the synthesis temperature caused a red shift of the PL peak wavelength for the prepared $CsPbBr_3$ NCs under the same total flow rate. From Fig. S2,† we note a blue shift of the PL peak wavelength for the prepared $CsPbBr_3$ NCs with the increase of the total flow rate at the same synthesis temperature. For example, the PL peak wavelength increases from 483 nm to 503 nm with the increase of the synthesis temperature from 303 to 363 K for the total flow rate of 6.3 mL min^{-1} and from 483 nm to 499 nm with the decrease of the total flow rate from 6.3 mL min^{-1} to 1.05 mL min^{-1} at the synthesis temperature of 303 K. Table 1 summaries the PL peak wavelength of the prepared $CsPbBr_3$ NCs.

Using the PL peak wavelength and the relation between the bandgap and the PL peak wavelength, $E = hc/\lambda q$ in the unit of eV (h, c, λ and q are the Planck constant, light speed in a vacuum, emission wavelength of photons and electron charge, respectively), the bandgaps of the prepared $CsPbBr_3$

 This journal is © The Royal Society of Chemistry 2022

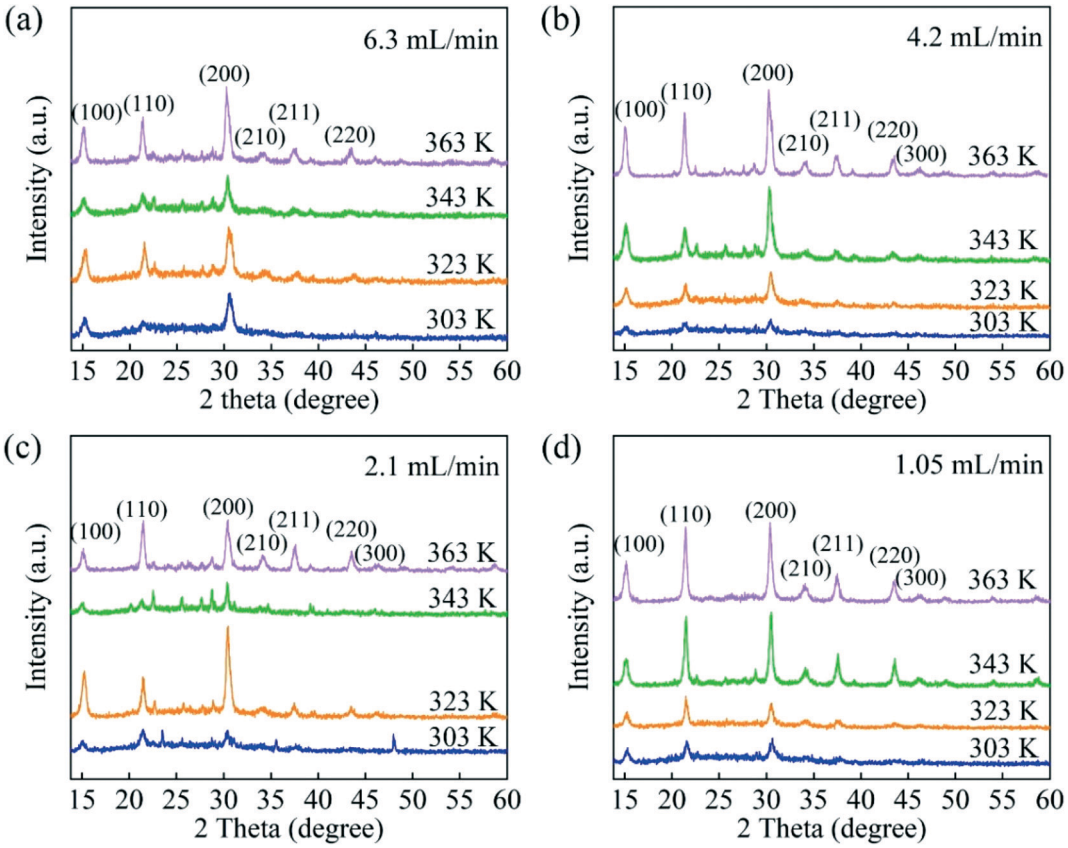

Fig. 3 XRD patterns of the $CsPbBr_3$ NCs prepared at four different temperatures of 303, 323, 343 and 363 K for different total flow rates of (a) 6.3 mL min^{-1}, (b) 4.2 mL min^{-1}, (c) 2.1 mL min^{-1}, and (d) 1.05 mL min^{-1}. The XRD patterns are in agreement with PDF card#54-0752.

NCs are calculated and listed in Table 1. It is evident that the bandgap decreases with the increase of the synthesis temperature for the same flow rate and with the decrease of the total flow rate at the same synthesis temperature. The repeated batch-to-batch preparation for the $CsPbBr_3$ NCs for 5 times reveals insignificant standard deviations of the PL-peak wavelength for the NCs prepared under the same conditions, suggesting reproducible nanocrystal synthesis.

Discussion

It is known that the PL peak wavelength of semiconductor NCs is dependent on the average size of the semiconductor NC, which can be referred to as the quantum confinement effect. According to the quantum confinement effect, the bandgap of a semiconductor NC, E, at temperature, T (absolute temperature), as a function of the characteristic size of the semiconductor NC, a, can be expressed as[56–58]

$$E(T) = E_0(T) + \frac{h^2}{2(m_e^* + m_h^*)}\frac{1}{a^2} \equiv E_0(T) + \frac{\alpha}{a^2} \quad (1)$$

where $E_0(T)$ is the bandgap of the bulk phase of the corresponding semiconductor at temperature, T, and m_e^* and m_h^* are the reduced masses of electrons and holes, respectively. Note that eqn (1) is based on the contribution of the Coulomb interaction to the bandgap of the semiconductor NC being negligible.

The variation of the PL peak wavelength of the prepared $CsPbBr_3$ NCs with the synthesis temperature and the total flow rate suggests the size dependence of the prepared $CsPbBr_3$ NCs on the synthesis temperature and the flow rate, *i.e.*, the growth of the $CsPbBr_3$ NCs in the microfluidic platform is dependent on the synthesis temperature and the growth time (flow rate). For a diffusion-dominant growth process, the time dependence of the characteristic size of a semiconductor NC can be expressed as[59,60]

$$a^2 = Dt \quad (2)$$

with D being the diffusion coefficient of monomers in the liquid solution, and t being the growth time. The temperature dependence of the diffusion coefficient follows the Arrhenius relation as

$$D = D_0 e^{-Q/RT} \quad (3)$$

where D_0 is a pre-factor, Q is the activation energy for the diffusion of the monomers in the liquid solution, and R is the gas constant.

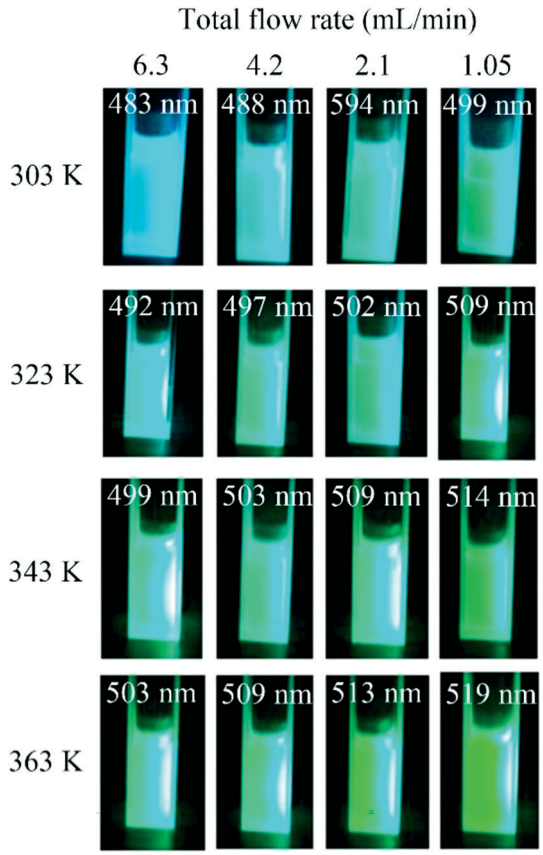

Fig. 4 Optical images of the suspensions of the prepared $CsPbBr_3$ NCs in cuvettes prepared with different flow rates at different temperatures under UV light of 365 nm wavelength.

Using the flow rates and the material properties (densities and viscosities) of DMF and toluene, we estimated the viscosity of the liquid suspensions and calculated the Reynolds numbers for the corresponding flow rates (Table S2 in the ESI†). The largest Reynolds number corresponding to the total flow rate of 6.3 mL min^{-1} is 266, suggesting that the flow in the microfluidic system is laminar for the flow rates used in this work. Note that the Reynolds number for the outset of the transition from laminar flow to turbulent flow is ~2300 for a pipe flow. Corresponding to the total flow rate of 6.3 mL min^{-1}, the average flow speed is 20.9 mm s^{-1}. Yang[61] noted a ~15% increase in the change of the Gibbs free energy for the average flow speed being increased from 2 mm s^{-1} to 20 mm s^{-1} in the study of homogeneous nucleation in a Poiseuille flow. This change suggests that the effect of convection on the growth of NCs in the microfluidic system is limited and the growth is not in a mass-transfer-limited regime. Thus, it is reasonable to assume that the contribution of convection from the flow to the growth of $CsPbBr_3$ NCs in the microfluidic system is negligible[61] and the growth time of the $CsPbBr_3$ NCs in the microfluidic platform is inversely proportional to the total flow rate, F, as

$$t \propto F^{-1} \tag{4}$$

Note that eqn (4) is based on the geometrical dimensions and structure of the microfluidic platform remaining unchanged for the growth conditions used in this work.

Substituting eqn (2)–(4) in eqn (1) yields

$$E(T) = E_0(T) + \beta e^{Q/RT} F \tag{5}$$

where β is a constant proportional to α and D_0^{-1}. Fig. 6 shows the variation of the bandgap of the prepared $CsPbBr_3$ NCs with the total flow rate at different synthesis temperatures. It is evident that the bandgap of the $CsPbBr_3$ NCs prepared at the same synthesis temperature is a linear function of the flow rate, supporting eqn (5). Using linear regression to fit the experimental results shown in Fig. 6, we obtain $E_0(T)$ and $\beta e^{Q/RT}$.

According to the relation given by Varshni,[62] the temperature dependence of the bandgap of a bulk semiconductor can be expressed as

$$E_0(T) = E_0 - \frac{bT^2}{T + c} \tag{6}$$

with E_0 being the bandgap of the semiconductor at 0 K, and b and c being two constants. It is known that bulk $CsPbBr_3$ can be presented in an orthorhombic, tetragonal and cubic structure in the temperature range of 0 to 353 K, 273 to 403 K and 403 K above, respectively.[63] That is to say, bulk $CsPbBr_3$ can be seldom presented in a cubic structure at 0 K. To estimate the numerical value of E_0 for cubic $CsPbBr_3$ at 0 K, we linearly extrapolate the numerical results given by Mannino *et al.*[64] and obtain $E_0 \approx 2.29$ eV.

Fig. 7 depicts the temperature dependence of $E_0(T) - E_0$. The bandgap of the bulk $CsPbBr_3$ of cubic structure exhibits a decreasing trend with the increase of the temperature. Eqn (6) is used to fit the data in Fig. 7. For comparison, the fitting curve is also included in Fig. 7. It is evident that eqn (6) describes well the temperature dependence of $E_0(T)$. From the curve fitting, we obtain $b = -6.99 \times 10^{-5}$ eV K^{-1} and $c = -267.84$ K for temperatures in the range of 303 to 363 K.

To determine the activation energy for the rate process controlling the growth of the $CsPbBr_3$ NCs in the microfluidic platform, we plot the temperature dependence of $\beta e^{Q/RT}$ in Fig. 8. It is evident that the logarithm of $\beta e^{Q/RT}$ is a linear function of T^{-1}. Using the linear relation between the logarithm of $\beta e^{Q/RT}$ and T^{-1} to fit the data in Fig. 8, we obtain an activation energy of 2.05 kJ mol^{-1} for the diffusion of monomers in the liquid solution under the flow environment, which controls the growth of the $CsPbBr_3$ NCs in the microfluidic platform for the conditions used in this work.

According to eqn (1), there is a linear relationship between the bandgap and the characteristic size of a semiconductor NC, which is the foundation for the above analysis. Fig. 9 depicts the variation of the bandgap with the reciprocal of the square of the average size of the $CsPbBr_3$ NCs formed in the microfluidic platform for the total flow rate of 1.05 mL min^{-1}. Both the average sizes of the $CsPbBr_3$ NCs determined

 This journal is © The Royal Society of Chemistry 2022

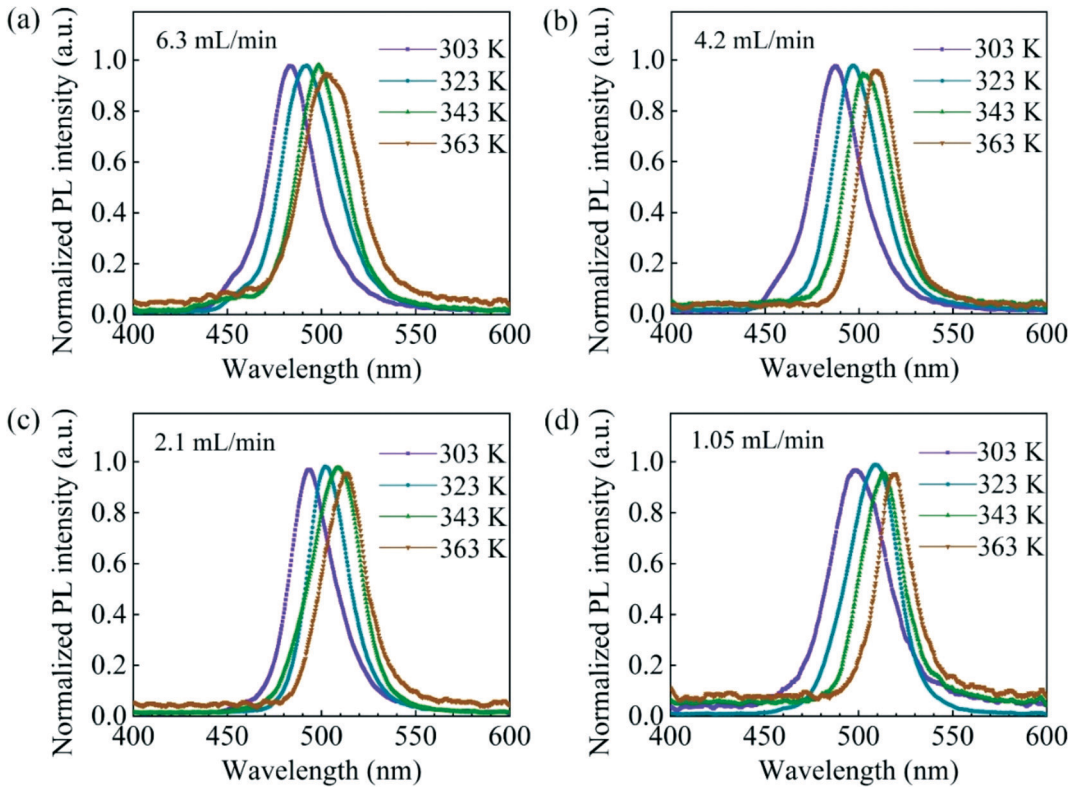

Fig. 5 PL spectra of the $CsPbBr_3$ NCs prepared at four different temperatures with different total flow rates under UV light of 365 nm wavelength: (a) 6.3 mL min^{-1}, (b) 4.2 mL min^{-1}, (c) 2.1 mL min^{-1}, and (d) 1.05 mL min^{-1}.

from the TEM images and XRD analyses are included in Fig. 9. In general, the bandgap is an approximately linearly increasing function of the reciprocal of the square of the average size of the $CsPbBr_3$ NCs in good accordance with eqn (1) for both groups of data. Such a result supports the method used in this work to analyze the growth behavior of the $CsPbBr_3$ NCs synthesized in the microfluidic platform. It needs to be pointed out that there are some differences between the average sizes of the $CsPbBr_3$ NCs determined from XRD and the corresponding ones determined from the TEM images. As discussed above, TEM images are two-dimensional without information of the crystal size in the depth direction and the average crystal size is calculated from two-dimensional information. TEM images only provide the information of local area with small amounts of samples. XRD patterns contain three-dimensional information from large amounts of samples, and the average crystal size is calculated from much larger numbers of crystals. Also, the centrifugation and drying for the preparation of the XRD samples might cause the coalescence of the $CsPbBr_3$ NCs, leading to the increase of the average crystal size determined from the XRD analyses.

In the following analysis, the average crystal sizes of the $CsPbBr_3$ NCs determined from the XRD analyses are used in the corresponding calculations. Using eqn (1), we have the bandgap difference at half maximum of the PL peak of the $CsPbBr_3$ NCs, ΔE_{FWHM}, as

$$\Delta E_{FWHM} = \frac{\alpha}{(a-\Delta a/2)^2} - \frac{\alpha}{(a+\Delta a/2)^2} \approx \frac{2\alpha\Delta a}{a^3} \quad (7)$$

for $a \gg \Delta a$. Here, Δa is the size difference between the $CsPbBr_3$ NCs at $E - \Delta E_{FWHM}/2$ and those at $E + \Delta E_{FWHM}/2$. It is evident that ΔE_{FWHM} is proportional to Δa, as revealed in eqn (7). Fig. 10 presents the variation of $\Delta E_{FWHM} \cdot a^3$ with the total flow rate. It is evident that the numerical values of $\Delta E_{FWHM} \cdot a^3$ for the $CsPbBr_3$ NCs prepared at the same temperature decrease with the increase of the total flow rate for all four temperatures of 303, 323, 343 and 363 K. Such a

Table 1 Wavelengths and bandgaps of the $CsPbBr_3$ NCs prepared at different flow rates and temperatures

	Wavelength (nm)/bandgap (eV)			
Temperature	6.3 mL min^{-1}	4.2 mL min^{-1}	2.1 mL min^{-1}	1.05 mL min^{-1}
303 K	483.3 ± 0.3/2.566 ± 0.003	488.3 ± 0.7/2.539 ± 0.007	493.7 ± 0.5/2.512 ± 0.005	499.0 ± 0.6/2.485 ± 0.006
323 K	491.9 ± 0.5/2.521 ± 0.005	497.2 ± 1.0/2.494 ± 0.010	502.4 ± 0.4/2.468 ± 0.004	509.3 ± 0.4/2.435 ± 0.004
343 K	499.3 ± 1.0/2.483 ± 0.010	502.5 ± 0.3/2.468 ± 0.003	509.3 ± 0.5/2.435 ± 0.005	514.0 ± 0.2/2.412 ± 0.002
363 K	503.3 ± 0.4/2.464 ± 0.004	509.2 ± 0.8/2.435 ± 0.008	512.9 ± 0.6/2.418 ± 0.006	519.0 ± 0.9/2.389 ± 0.009

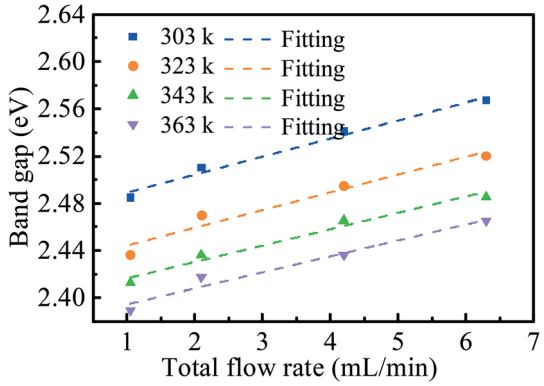

Fig. 6 Variation of the bandgap of the prepared $CsPbBr_3$ NCs with the total flow rate at different synthesis temperatures.

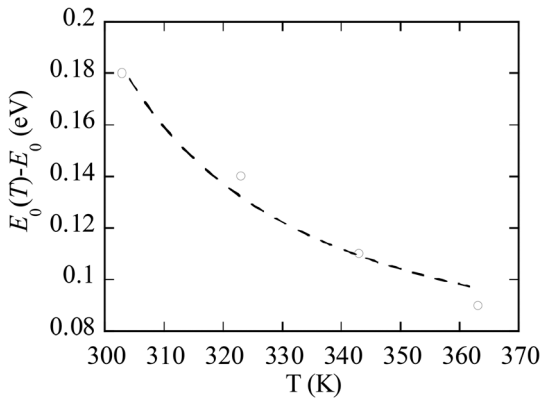

Fig. 7 Temperature dependence of $E_0(T) - E_0$ for the prepared $CsPbBr_3$ NCs.

trend reveals that the total flow rate plays a role in the dispersity of the $CsPbBr_3$ NCs grown in the microfluidic system. The higher the total flow rate, the small the dispersity of the $CsPbBr_3$ NCs. From Fig. 10, we note that increasing the growth temperature generally caused the increase of the numerical values of $\Delta E_{FWHM}{\cdot}a^3$ for the same total flow, indicating the increase of the dispersity of the

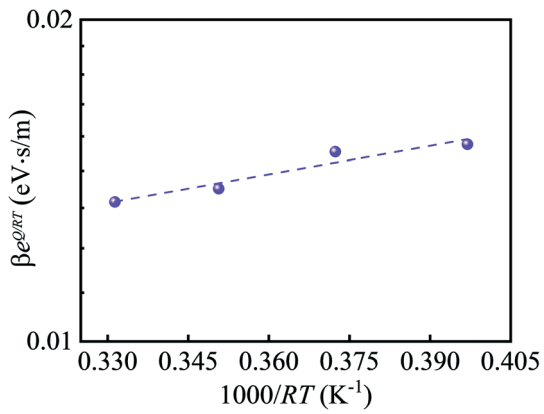

Fig. 8 Temperature dependence of $\beta e^{Q/RT}$ for the prepared $CsPbBr_3$ NCs.

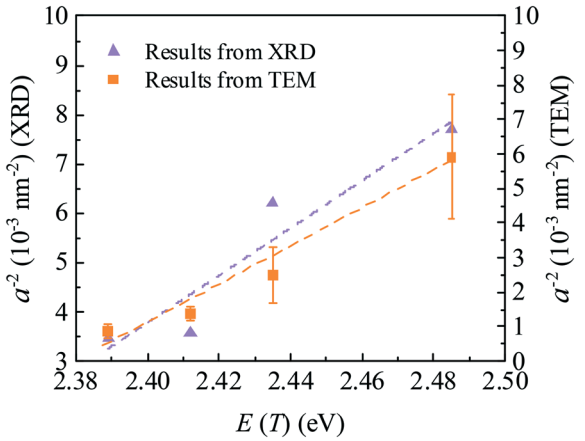

Fig. 9 Size dependence of the bandgap.

$CsPbBr_3$ NCs grown at high temperatures. Note that the numerical value of $\Delta E_{FWHM}{\cdot}a^3$ for the $CsPbBr_3$ NCs grown at 363 K is larger than that grown at 343 K for the total flow rate of 1.05 mL min^{-1}. The reason for such an opposite trend is unclear, and it might be due to experimental errors.

There are two process variables controlling the growth time: one is the total flow rate and the other is the capillary length between the miniaturized reactor and the large glass vial. Increasing the capillary length and decreasing the total flow rate can increase the growth time of $CsPbBr_3$ NCs. To evaluate the effects of the capillary length between the miniaturized reactor and the large glass vial on the PL characteristics and the size evolution of $CsPbBr_3$ NCs, we prepared $CsPbBr_3$ NCs from the same microfluidic system with different capillary lengths (20, 40, 60 and 80 cm) between the miniaturized reactor and the large glass vial for a total flow rate of 1.05 mL min^{-1} at 303 K. Fig. S3 and S4† present the PL spectra and XRD patterns of the $CsPbBr_3$ NCs prepared with four different capillary lengths. The corresponding PL peak wavelengths and average crystal sizes of the prepared $CsPbBr_3$ NCs are summarized in Table 2.

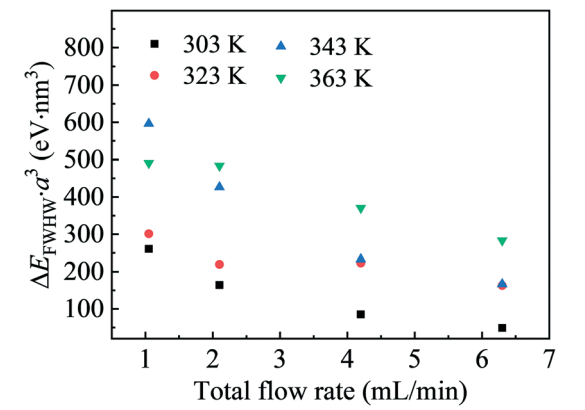

Fig. 10 Variation of $\Delta E_{FWHM}{\cdot}a^3$ with the total flow rate for the $CsPbBr_3$ NCs prepared at different temperatures. Here, the average crystal sizes of the $CsPbBr_3$ NCs determined from the XRD analyses are used in the calculation.

This journal is © The Royal Society of Chemistry 2022

Table 2 PL peak wavelengths and average crystal sizes of the $CsPbBr_3$ NCs prepared for a total flow rate of 1.05 mL min^{-1} at 303 K with four different capillary lengths

		Wavelength (nm)/average size (nm)			
Temperature	Flow rate	20 cm	40 cm	60 cm	80 cm
303 K	1.05 mL min^{-1}	493.2 ± 1.0/10.1	497.1 ± 0.4/10.9	499.5 ± 0.5/11.5	502.3 ± 0.9/12.0

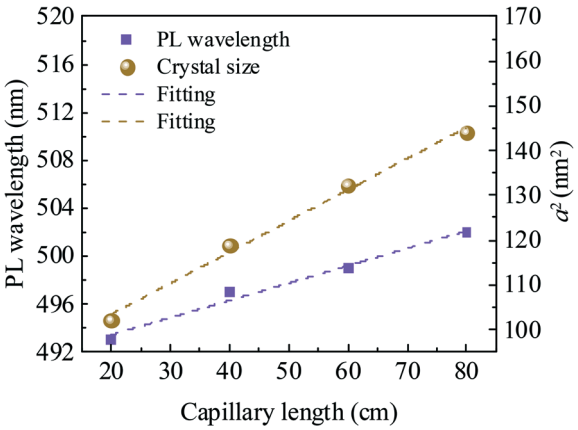

Fig. 11 Variations of PL peak wavelength and square of average crystal size of the $CsPbBr_3$ NCs prepared with different capillary lengths (total flow rate: 1.05 mL min^{-1}, temperature: 303 K).

Using the experimental data in Table 2, the variations of the PL peak wavelength and the square of the average crystal size with the capillary length are depicted in Fig. 11. It is evident that both the PL peak wavelength and the square of average crystal size are linearly increasing functions of the capillary length, suggesting the linear correlation between the PL peak wavelength (reciprocal of the bandgap) and the square of the average crystal size. This result supports eqn (1) for the $CsPbBr_3$ NCs grown under the same growth conditions with different capillary lengths. For a constant total flow rate, the time for the $CsPbBr_3$ NCs grown in the microfluidic system is a linearly increasing function of the capillary length. Thus, there exists a linear relation between the growth time and the square of average crystal size, which again suggests the diffusion of monomers as the dominant mechanism for the growth of $CsPbBr_3$ NCs in the microfluidic system.

Conclusion

Microfluidics has provided a platform to continuously fabricate nanoparticles and semiconductor nanocrystals. We have used a PTFE-based microfluidic system and the antisolvent principle to continuously synthesize $CsPbBr_3$ NCs in a temperature range of 303 to 363 K for the total flow rates of 1.05, 2.1, 4.2 and 6.3 mL min^{-1}. Both the TEM and XRD analyses have confirmed the production of $CsPbBr_3$ NCs of cubic structure and found the dependence of the average size of the prepared $CsPbBr_3$ NCs on the synthesis conditions, including the flow rate, the capillary length and the synthesis temperature. There exist differences in the average sizes of the prepared $CsPbBr_3$ NCs with the total flow rate of 1.05 mL min^{-1} between the results from the TEM analysis and those from the XRD analysis. Such differences can be attributed to the difference in the sampling sizes and the possible coalescence of NCs during the centrifugation and drying – TEM images were obtained from limited amounts of NCs and captured two-dimensional features of NCs, and XRD analyses used significantly large amounts of NCs which might experience coalescence during the centrifugation and drying.

We have developed a relationship between the bandgap (the PL peak wavelength) and the total flow rate (the growth time) for the growth of semiconductor nanocrystals in a microfluidic system from the size-dependence of the bandgap of semiconductor NCs (the quantum confinement effect) under the condition that the contribution of the Coulomb interaction to the quantum confinement is negligible. Using this relationship and the PL characteristics of the prepared $CsPbBr_3$ NCs, we have analyzed the growth behavior of the $CsPbBr_3$ NCs prepared in the microfluidic system and found the proportionality between the reciprocal of the square of the average size of the $CsPbBr_3$ NCs and the total flow rate and between the square of the average size of the $CsPbBr_3$ NCs and the capillary length between the miniaturized reactor and the NC-collection outlet. Such results suggest that the diffusion of monomers in the liquid solution is the dominant rate process controlling the growth of the $CsPbBr_3$ NCs in the microfluidic system. The activation energy for the rate process is 2.05 kJ mol^{-1}, and the temperature dependence of the bandgap of the bulk $CsPbBr_3$ crystals of cubic structure follows the empirical relation developed by Varshni.[62]

We have derived a relation between the difference of the bandgaps at half maximum of the PL peak and the corresponding size difference from the relation between the bandgap and the average size of semiconductor NCs. Using this relation, we have analyzed the effects of the synthesis temperature and the total flow rate on the size distribution of the prepared $CsPbBr_3$ NCs. The analysis reveals that increasing the synthesis temperature widens the size distribution of the $CsPbBr_3$ NCs prepared in the microfluidic platform.

It is worth mentioning that the relationship between the bandgap (the PL peak wavelength) and the total flow rate (the growth time) for the growth of semiconductor nanocrystals provides the basis to analyze the growth behavior of semiconductor nanocrystals under dynamic conditions from *in situ* measurement of the PL characteristics of the

semiconductor nanocrystals. Such an approach avoids the use of TEM and XRD techniques, which likely involve the coalescence of semiconductor nanocrystals during the sample processing and/or under e-beam and X-ray and limited amounts of NCs used in TEM imaging, and can be extended to *in situ* study the growth behavior of other semiconductor nanocrystals under a variety of synthesis conditions.

Conflicts of interest

The authors declare no conflict of interest.

Acknowledgements

FY is grateful for the support by the NSF through the grant CMMI-1854554, monitored by Drs. Khershed Cooper and Thomas Francis Kuech, and CBET-2018411 monitored by Dr. Nora F Savage.

References

1 E. K. Sackmann, A. L. Fulton and D. J. Beebe, *Nature*, 2014, **507**, 181–189.
2 X. Mao and T. J. Huang, *Lab Chip*, 2012, **12**, 1412–1416.
3 D. R. Walt, *Science*, 2005, **308**, 217–219.
4 Y. Xia, J. Si and Z. Li, *Biosens. Bioelectron.*, 2016, **77**, 774–789.
5 M. L. Adams, M. Enzelberger, S. Quake and A. Scherer, *Sens. Actuators, A*, 2003, **104**, 25–31.
6 Y. Zilberman, S. K. Ameri and S. R. Sonkusale, *Sens. Actuators, B*, 2014, **194**, 404–409.
7 C. M. B. Ho, S. H. Ng, K. H. H. Li and Y.-J. Yoon, *Lab Chip*, 2015, **15**, 3627–3637.
8 A. K. Au, W. Huynh, L. F. Horowitz and A. Folch, *Angew. Chem., Int. Ed.*, 2016, **55**, 3862–3881.
9 A. V. Nielsen, M. J. Beauchamp, G. P. Nordin and A. T. Woolley, *Annu. Rev. Anal. Chem.*, 2020, **13**, 45–65.
10 A. Jahn, J. E. Reiner, W. N. Vreeland, D. L. DeVoe, L. E. Locascio and M. Gaitan, *J. Nanopart. Res.*, 2008, **10**, 925–934.
11 D. Desai, Y. A. Guerrero, V. Balachandran, A. Morton, L. Lyon, B. Larkin and D. E. Solomon, *Nanomed.: Nanotechnol., Biol. Med.*, 2021, 102402.
12 L. Protesescu, S. Yakunin, M. I. Bodnarchuk, F. Krieg, R. Caputo, C. H. Hendon, R. X. Yang, A. Walsh and M. V. Kovalenko, *Nano Lett.*, 2015, **15**, 3692–3696.
13 F. P. García de Arquer, D. V. Talapin, V. I. Klimov, Y. Arakawa, M. Bayer and E. H. Sargent, *Science*, 2021, **373**, eaaz8541.
14 Q. A. Akkerman, G. Rainò, M. V. Kovalenko and L. Manna, *Nat. Mater.*, 2018, **17**, 394–405.
15 W. Chi and S. Banerjee, *Angew. Chem.*, 2022, **134**, e202112412.
16 Y. Bai, M. Hao, S. Ding, P. Chen and L. Wang, *Adv. Mater.*, 2021, 2105958.
17 Y. Wei, Z. Cheng and J. Lin, *Chem. Soc. Rev.*, 2019, **48**, 310–350.
18 J. Shamsi, A. S. Urban, M. Imran, L. De Trizio and L. Manna, *Chem. Rev.*, 2019, **119**, 3296–3348.
19 Y. He, L. Matei, H. J. Jung, K. M. McCall, M. Chen, C. C. Stoumpos, Z. Liu, J. A. Peters, D. Y. Chung and B. W. Wessels, *Nat. Commun.*, 2018, **9**, 1–8.
20 D. N. Dirin, I. Cherniukh, S. Yakunin, Y. Shynkarenko and M. V. Kovalenko, *Chem. Mater.*, 2016, **28**, 8470–8474.
21 I. G. Koryakina, M. Naumochkin, D. I. Markina, S. A. Khubezhov, A. P. Pushkarev, A. A. Evstrapov, S. V. Makarov and M. V. Zyuzin, *Chem. Mater.*, 2021, **33**, 2777–2784.
22 Z. Bao, J.-W. Luo, Y.-S. Wang, T.-C. Hu, S.-Y. Tsai, Y.-T. Tsai, H.-C. Wang, F.-H. Chen, Y.-C. Lee and T.-L. Tsai, *Chem. Eng. J.*, 2021, 130849.
23 C. Zhang, W. Luan, Y. Huang and F. Yang, *Nanotechnology*, 2019, **30**, 145602.
24 S. Marre and K. F. Jensen, *Chem. Soc. Rev.*, 2010, **39**, 1183–1202.
25 S. Kubendhiran, Z. Bao, K. Dave and R.-S. Liu, *ACS Appl. Nano Mater.*, 2019, **2**, 1773–1790.
26 R. W. Epps, K. C. Felton, C. W. Coley and M. Abolhasani, *Lab Chip*, 2017, **17**, 4040–4047.
27 I. Lignos, S. Stavrakis, G. Nedelcu, L. Protesescu, A. J. deMello and M. V. Kovalenko, *Nano Lett.*, 2016, **16**, 1869–1877.
28 K. Ma, X.-Y. Du, Y.-W. Zhang and S. Chen, *J. Mater. Chem. C*, 2017, **5**, 9398–9404.
29 K. Abdel-Latif, R. W. Epps, F. Bateni, S. Han, K. G. Reyes and M. Abolhasani, *Adv. Intell. Syst.*, 2021, **3**, 2000245.
30 S. Li, R. W. Baker, I. Lignos, Z. Yang, S. Stavrakis, P. D. Howes and A. J. deMello, *Mol. Syst. Des. Eng.*, 2020, **5**, 1118–1130.
31 Y. Geng, J. Guo, S. D. Ling, X. Wu, H. Liu, Z. Chen, S. Chen and J. Xu, *Sci. China Mater.*, 2022, 1–9.
32 R. Guo, Y. Liu, Y. Fang, Z. Liu, L. Dong, L. Wang, W. Li and J. Hou, *CrystEngComm*, 2022, **24**, 3852–3858.
33 Z. Bao, H.-C. Wang, Z.-F. Jiang, R.-J. Chung and R.-S. Liu, *Inorg. Chem.*, 2018, **57**, 13071–13074.
34 Y. Yu, J. Guo, F. Bian, D. Zhang and Y. Zhao, *Sci. China Mater.*, 2021, **64**, 2858–2867.
35 R. Cheng, Z. B. Liang, L. Zhu, H. Li, Y. Zhang, C. F. Wang and S. Chen, *Angew. Chem.*, 2022, e202204371.
36 F. Bian, L. Sun, Y. Wang, D. Zhang, Z. Li and Y. Zhao, *Sci. China: Chem.*, 2021, **64**, 1540–1546.
37 K. Abdel-Latif, R. W. Epps, C. B. Kerr, C. M. Papa, F. N. Castellano and M. Abolhasani, *Adv. Funct. Mater.*, 2019, **29**, 1900712.
38 S.-M. Kang, B. Park, G. S. R. Raju, S. Baek, S. K. Hussain, C. H. Kwak, Y.-K. Han, J. S. Yu, S.-W. Kim and Y. S. Huh, *Chem. Eng. J.*, 2020, **384**, 123316.
39 R. M. Maceiczyk, L. Bezinge and A. J. deMello, *React. Chem. Eng.*, 2016, **1**, 261–271.
40 Y. Tang, H. Lu, L. Rao, Z. Li, X. Ding, C. Yan and B. Yu, *Materials*, 2018, **11**, 371.
41 Z. Zhang, Y. Liu, C. Geng, S. Shi, X. Zhang, W. Bi and S. Xu, *Nanoscale*, 2019, **11**, 18790–18796.
42 R. M. Maceiczyk, K. Dümbgen, I. Lignos, L. Protesescu, M. V. Kovalenko and A. J. deMello, *Chem. Mater.*, 2017, **29**, 8433–8439.

 This journal is © The Royal Society of Chemistry 2022

43 I. Lignos, L. Protesescu, D. B. R. Emiroglu, R. Maceiczyk, S. Schneider, M. V. Kovalenko and A. J. deMello, *Nano Lett.*, 2018, **18**, 1246–1252.

44 I. Lignos, V. Morad, Y. Shynkarenko, C. Bernasconi, R. M. Maceiczyk, L. Protesescu, F. Bertolotti, S. Kumar, S. T. Ochsenbein and N. Masciocchi, *ACS Nano*, 2018, **12**, 5504–5517.

45 L. Bezinge, R. M. Maceiczyk, I. Lignos, M. V. Kovalenko and A. J. deMello, *ACS Appl. Mater. Interfaces*, 2018, **10**, 18869–18878.

46 F. Yang, *Eur. Phys. J.: Appl. Phys.*, 2022, **97**, 20.

47 M. R. Karim, M. Balaban and H. Unlu, *Adv. Mater. Sci. Eng.*, 2019, **2019**, 3764395.

48 X. Li, Y. Wu, S. Zhang, B. Cai, Y. Gu, J. Song and H. Zeng, *Adv. Funct. Mater.*, 2016, **26**, 2435–2445.

49 Z. Wei, Y. Chen, P. Lin, Q. Yan, Y. Fan and Z. Cheng, *J. Mater. Sci.*, 2019, **54**, 6841–6852.

50 P. Lin, H. Chen, Z. Wei, Y. Lin, J. Lin, Y. Chen and Z. Cheng, *Sci. China Mater.*, 2020, **63**, 1526–1536.

51 C. K. Ng, H. Deng, H. Li, W. Yin, T. Alan and J. J. Jasieniak, *J. Mater. Chem. C*, 2021, **9**, 313–321.

52 F. Zhang, H. Zhong, C. Chen, X.-G. Wu, X. Hu, H. Huang, J. Han, B. Zou and Y. Dong, *ACS Nano*, 2015, **9**, 4533–4542.

53 Y. Zhang, T. D. Siegler, C. J. Thomas, M. K. Abney, T. Shah, A. De Gorostiza, R. M. Greene and B. A. Korgel, *Chem. Mater.*, 2020, **32**, 5410–5423.

54 P.-H. Haumesser, *Nucleation and growth of metals: from thin films to nanoparticles*, Elsevier, ISTE Press, London, UK, 2016.

55 A. A. Al-Tabbakh, N. Karatepe, A. B. Al-Zubaidi, A. Benchaabane and N. B. Mahmood, *Int. J. Energy Res.*, 2019, **43**, 1903–1911.

56 E. Hanamura, in *Confined Electrons and Photons*, Springer, New York, 1995, pp. 831–837.

57 Z. Fu, Y. Cui, S. Zhang, J. Chen, D. Yu, S. Zhang, L. Niu and J. Jiang, *Appl. Phys. Lett.*, 2007, **90**, 263113.

58 F. Yang, *Phys. Lett. A*, 2021, **401**, 127346.

59 F. Yang, *Langmuir*, 2021, **37**, 3912–3921.

60 C. Fanelli, V. Cregan, F. Font and T. Myers, *Int. J. Heat Mass Transfer*, 2021, **165**, 120643.

61 F. Yang, *Phys. Chem. Chem. Phys.*, 2021, **23**, 3974–3982.

62 Y. P. Varshni, *Physica*, 1967, **34**, 149–154.

63 M. Ezzeldien, S. Al-Qaisi, Z. Alrowaili, M. Alzaid, E. Maskar, A. Es-Smairi, T. V. Vu and D. Rai, *Sci. Rep.*, 2021, **11**, 1–12.

64 G. Mannino, I. Deretzis, E. Smecca, A. La Magna, A. Alberti, D. Ceratti and D. Cahen, *J. Phys. Chem. Lett.*, 2020, **11**, 2490–2496.

This journal is © The Royal Society of Chemistry 2022